

Velocity dispersion in rocks: A laboratory technique for direct measurement of P-wave modulus at seismic frequencies

Serhii Lozovyi ^{1,2}

Andreas Bauer ^{1,2}

¹ Department of Geoscience and Petroleum, Norwegian University of Science and Technology (NTNU), Trondheim, 7031, Norway

² Petroleum Department, SINTEF, Trondheim, 7031, Norway

Abstract

Fluid saturated rocks exhibit a dependence of acoustic velocities on frequency, which is called velocity dispersion. For some rocks, e.g. shales, velocity dispersion is rather strong and have to be taken into account when interpreting and comparing data from seismic surveys, sonic logs, and ultrasonic measurements on core plugs in the laboratory. In this work, a new laboratory technique has been developed that allows the direct measurement of the P-wave modulus at seismic frequencies from which P-wave velocities can be derived. Together with ultrasonic velocity measurements that are carried out simultaneously, the P-wave velocity dispersion between seismic and ultrasonic frequencies is obtained.

Keywords

Velocity dispersion, P-wave modulus, shale, transverse isotropy

I. Introduction

Seismic methods of subsurface imaging are used for exploration and monitoring of oil & gas production, CO₂ and nuclear waste storage, and applied for large areas and depths that are not easily accessible. For the interpretation of seismic data, the elastic rock properties have to be known. Conventionally, rock acoustic velocities (and derived elastic properties) are measured at ultrasonic frequencies (>100 kHz) in the laboratory, or at sonic frequencies (kHz range) in the borehole (sonic logs). These properties are then used to interpret the seismic survey data that is recorded as seismic frequencies (1-100 Hz). Velocity dispersion (velocity change with frequency) is often neglected. However, several studies show that dispersion between seismic and ultrasonic frequencies can be significant (Winkler and Nur, 1979; Duranti et al., 2005; Batzle et al., 2006) which may introduce significant errors in the interpretation. In addition, there are evidences that the velocity dispersion is dependent on stress and the degree of fluid saturation (Szewczyk et al., 2017, 2018), which will have an effect on time-lapse seismic (Hatchell and Bourne, 2005; Røste et al., 2007). Dispersion is also one of the key parameters for linking static and dynamic moduli of rocks (Fjær et al., 2011; Holt et al., 2013).

For the direct measurement of acoustic wave velocities, a sample has to be at least as long as half the wavelength (standing wave measurements; Murphy (1982)) or longer (pulse-transmission measurements; Winkler and Plona (1982)). Since wavelengths of seismic waves in rocks are much longer than a typical rock sample, direct measurements of seismic velocities are not possible in the laboratory. There is, however, a direct relationship between the dynamic stiffness and density of a material and its velocity. Seismic velocities can therefore be determined by measuring the material's density and dynamic stiffness at seismic frequencies, by assuming that the material is homogeneous, and the stiffness measured with a small sample is representative for the material's stiffness on the wavelength scale. The dynamic stiffness is

measured by applying small-amplitude stress oscillations to the sample at seismic frequencies, and measuring the strain modulation. Even though this low-frequency technique is known for a long time, only a few groups have applied it (see e.g. Jackson et al., 1984; Spencer, 1981; Getting et al., 1990; Batzle et al., 2006; Tisato and Madonna, 2012; Mikhaltsevitch et al., 2014; Pimienta et al., 2015; Szewczyk et al., 2016). Subramaniyan et al., (2014) provide a comprehensive overview over different dispersion and attenuation measurement techniques at seismic frequencies. Experimentally, the low-frequency technique is challenging because of the small stress and strain amplitudes: Strain-modulation amplitudes should be kept below 10^{-6} in order to remain in the linear-elastic regime (Winkler et al., 1979; Batzle et al., 2006; Lozovyi et al., 2017). This requires very sensitive equipment to acquire the signals. In addition, procedures of sealing and mounting the sample into the pressure cell are complicated due to use of strain gages attached to the sample surface.

Another issue of the low-frequency technique is sealing of a sample from a confining fluid in a pressure cell. The sample is equipped with strain gages and feeding out the wires requires special procedures. In addition, mounting time is very limited when working with saturated samples to preserve their initial saturation.

The most convenient way to measure the dynamic stiffness of a sample is to apply axial stress (σ_{ax}) and measure axial (ϵ_{ax}) and radial (ϵ_{rad}) strains. Young's modulus (E) and Poisson's ratio (ν) are the stiffness parameters that can be calculated directly:

$$E = \frac{\sigma_{ax}}{\epsilon_{ax}}; \nu = \frac{\epsilon_{rad}}{\epsilon_{ax}} \quad (1.1)$$

For isotropic rocks, the compressional (V_P) and shear (V_S) wave velocities can be calculated from the density of the sample (ρ) together with two independent stiffness parameters (Mavko et al., 2009):

$$\begin{aligned}
 V_p &= \sqrt{\frac{H}{\rho}} = \sqrt{\frac{E(1-\nu)}{\rho(1-2\nu)(1+\nu)}} \\
 V_s &= \sqrt{\frac{G}{\rho}} = \sqrt{\frac{E}{2\rho(1+\nu)}}
 \end{aligned}
 \tag{1.2}$$

where H is P-wave modulus, G is shear modulus.

For anisotropic rocks the stiffness is characterized by more than two independent parameters. P- and S-wave velocities, as well as Young's modulus and Poisson's ratio are direction dependent, and Eq. 1.2 is not applicable. Shales, the most abundant sedimentary rocks, often can be described as being transversely isotropy (TI) (Sayers, 2005). The stiffness tensor of a medium with TI symmetry contains five independent stiffness parameters and can be written in the following form using Voigt's notation (Nye, 1984):

$$\vec{\sigma} = \begin{pmatrix} C_{11} & C_{11} - 2C_{66} & C_{13} & 0 & 0 & 0 \\ C_{11} - 2C_{66} & C_{11} & C_{13} & 0 & 0 & 0 \\ C_{13} & C_{13} & C_{33} & 0 & 0 & 0 \\ 0 & 0 & 0 & C_{44} & 0 & 0 \\ 0 & 0 & 0 & 0 & C_{44} & 0 \\ 0 & 0 & 0 & 0 & 0 & C_{66} \end{pmatrix} \cdot \vec{\varepsilon}
 \tag{1.3}$$

Here, C_{11} , C_{33} , C_{44} , C_{66} , and C_{13} are the five independent stiffness parameters. Using conventional triaxial cells that allow for the application of a confining pressure and an axial stress (biaxial stress conditions), measurements with three differently oriented samples are needed to determine all five stiffness parameters. In the present work, measurements were done with core plugs with the following orientations: bedding planes perpendicular (0°), under an angle of 45° (45°), and parallel (90°) to the sample axis (see Figure 1).

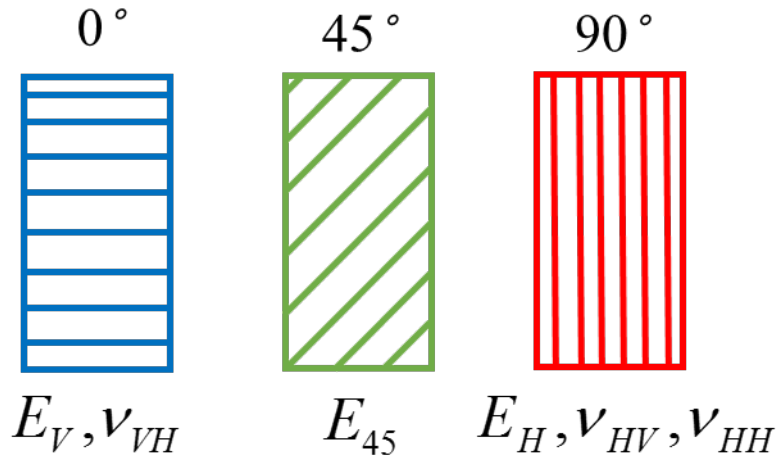


Figure 1. Sample orientations and corresponding stiffness parameters that are measured with conventional low-frequency technique with uniaxial stress conditions for transversely isotropic rocks (shales).

Figure 1 also shows the parameters that are measured with the different samples. E_V , E_H , and E_{45} are the Young moduli for uniaxial stress applied perpendicular (V), parallel (H), and under 45° (45) with respect to bedding, respectively. For the Poisson's ratios, ν_{VH} , ν_{HV} , ν_{HH} , the first index denotes the direction of the applied uniaxial stress (V – vertical, perpendicular to bedding, H – horizontal, parallel to bedding), and the second index denotes the direction in which the strain is measured.

From the measured parameters (E_V , E_H , E_{45} , ν_{VH} , ν_{HV} , ν_{HH}) the stiffness parameters C_{11} , C_{33} , C_{44} , C_{66} , and C_{13} can be calculated (Bower, 2010; Nye, 1984):

$$\begin{aligned}
 C_{33} &= E_V(1 - \nu_{HH}^2) \Lambda \\
 C_{44} &= \left(\frac{4}{E_{45}} - \frac{1}{E_V} - \frac{1}{E_H} + \frac{C_{13}}{(C_{11} - C_{66})C_{33} - C_{13}^2} \right)^{-1} \\
 C_{11} &= E_H(1 - \nu_{HV}\nu_{VH}) \Lambda \\
 C_{66} &= E_H / 2(1 + \nu_{HH}) \\
 C_{13} &= E_H\nu_{VH}(1 + \nu_{HH}) \Lambda \\
 \Lambda &= \left(1 - \nu_{HH}^2 - 2\nu_{HV}\nu_{VH} - 2\nu_{HV}\nu_{VH}\nu_{HH} \right)^{-1}
 \end{aligned} \tag{1.4}$$

The number of independent parameters for TI medium is 5, but the low-frequency setup allows for measuring 6 parameters (Figure 1). It can be shown that (Sayers, 2012):

$$\left(\frac{E_V}{E_H} \right) \Big/ \left(\frac{v_{VH}}{v_{HV}} \right) = 1 \quad (1.5)$$

Deviations from the unity of the ratio of the ratios in Eq. (1.5) will indicate a deviation from TI symmetry or differences in properties of 0° and 90° oriented samples caused by heterogeneities in the rock.

Further, the stiffness parameters relate to wave velocities as follows:

$$\begin{aligned} \rho v_{PV}^2 &= C_{33} \\ \rho v_{PH}^2 &= C_{11} \\ \rho v_{SV}^2 &= C_{44} \\ \rho v_{SH}^2 &= C_{66} \end{aligned} \quad (1.6)$$

Here, V_{PV} and V_{PH} denote velocities of P-waves perpendicular to bedding and parallel to bedding, respectively, V_{SV} is the velocity of an S-wave perpendicular to bedding, and V_{SH} is the velocity of an S-wave parallel to bedding with the polarization parallel to bedding. As it is seen from equations (1.4), the P-wave moduli C_{33} and C_{11} , as well as the S-wave modulus C_{66} depend on Young's moduli and Poisson's ratios measured with 0° and 90° oriented samples, and the S-wave modulus C_{44} depends on Young's moduli and Poisson's ratios for all three sample orientations. Large errors may occur if the differently oriented samples do not have identical mechanical properties due to rock heterogeneity, or if there are errors in the sample orientation (sometimes it is difficult to identify the bedding orientation, or the bedding orientation varies within the core material the samples are taken from). Errors in seismic velocities will also result in errors when comparing seismic and ultrasonic velocities (the latter

are measured directly with a single sample) and determining the magnitude of velocity dispersion.

Errors can be reduced if the seismic P- or S-wave moduli and ultrasonic velocities are directly measured with a single sample. In this work, we show how the P-wave modulus C_{33} can be measured directly with a 0° core plug at low frequencies. The measurements require uniaxial strain conditions, $\varepsilon_{rad}=0$. It is achieved by controlling both radial and axial stress at a given modulation frequency. If the condition $\varepsilon_{rad}=0$ is fulfilled, then C_{33} is given by:

$$C_{33} = \left. \frac{\sigma_{ax}}{\varepsilon_{ax}} \right|_{\varepsilon_{rad}=0} \quad (1.7)$$

A specially designed hydraulic cylinder unit is used to apply confining pressure oscillations and achieve uniaxial strain conditions during the low-frequency measurements in a triaxial cell. From the measured axial-strain and axial stress amplitudes, according to Eq. 1.7, the P-wave modulus C_{33} is obtained with a small error. To our knowledge, such measurements have not been done before.

In this paper, we discuss technical details of the low-frequency apparatus developed at SINTEF. Sections II and III give detailed description of the apparatus and a comprehensive error analysis; Chapter IV describes the new measurement technique for direct P-wave modulus measurements aimed to decrease errors in measuring velocity dispersion in transversely isotropic rocks (e.g. shales).

II. Low-frequency apparatus

The low-frequency apparatus (Figure 2) represents a conventional triaxial cell which is equipped with low frequency module for dynamic stress oscillations (frequency range 0.1-150 Hz), and P- and S-wave ultrasonic transducers (500 kHz). The setup allows for independent

control of confining pressure, vertical stress and pore pressure. The cell is designed for testing cylindrical samples of 1" in diameter and 2" in length (Figure 3).

A big advantage of the setup is the short sample-mounting time: the whole procedure takes 2-4 hours until the system is ready to be pressurised. The sample is exposed to air for about 20 to 40 minutes, most of which it is partially covered with rubber sleeve from the sides and endcaps from top and bottom. This allows to preserve the initial fluid saturation level of the sample which is crucial when studying preserved field samples or re-saturated outcrop samples.

The principle, design, and operation of the low-frequency apparatus will be discussed in following sub-chapters.

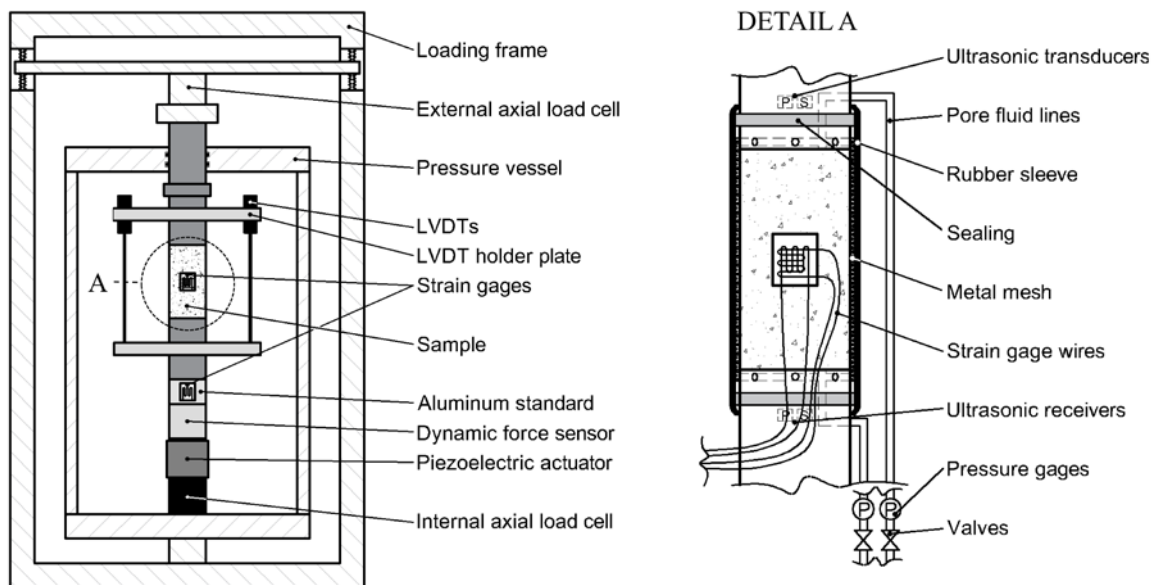


Figure 2. The low-frequency apparatus at SINTEF, Norway. Schematics of the apparatus configuration for standart uniaxial force oscillation test. Metal mesh around the sample is used when low permeability samples (e.g. shales) are tested.

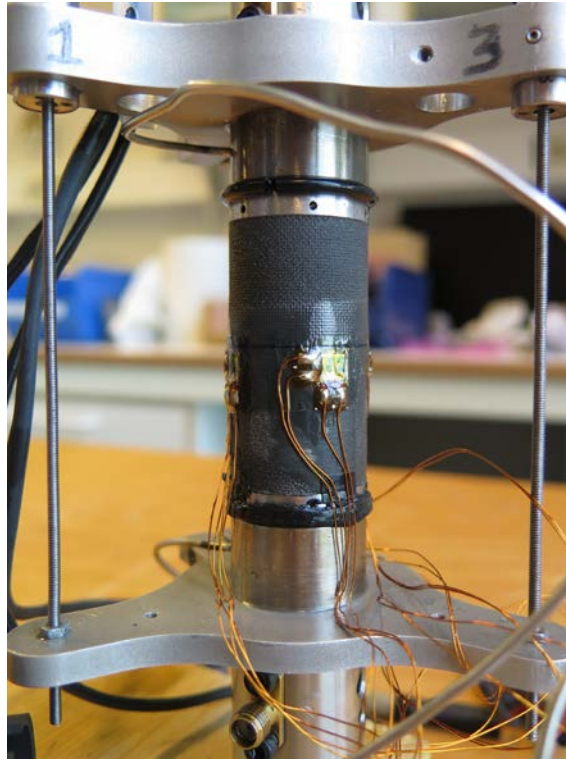


Figure 3. Photograph of a shale sample with attached strain gages after an experiment. A rubber sleeve and a metal mesh have been removed.

A. Static Stresses and Strains

Two Quizix QX6000 fluid pumps are used to control the confining (P_{conf}) and pore (P_f) pressures in the cell. The vertical axial stress (σ_{ax}) is applied by an electromechanical frame (MTS Criterion C45 300kN). The cell is designed for confining pressures and pore pressures up to 70 MPa, and the deviatoric stress ($\sigma_{\text{dev}} = \sigma_{\text{ax}} - P_{\text{conf}}$) is limited to 37 MPa (yield strength of the dynamic force sensor). The pore pressure is limited by the pump capability of about 50 MPa.

The confining pressure is measured both by an internal Quizix-pump pressure sensor, and a separate pressure sensor (HBM P2VA1-500) that is directly connected to the pressure vessel. The pore pressure is also measured by the pore-pressure pump as well as by two pressure sensors (Kistler 4075A500). The latter are integrated in the pore-fluid lines connected to the

top and bottom endcaps of the sample. The vertical axial stress is measured by a sensor integrated in the MTS loading frame, and the deviatoric stress ($\sigma_{\text{dev}} = \sigma_{\text{ax}} - P_{\text{conf}}$) is measured by an internal load cell (MetaRock SCL1-30K) that is placed inside the pressure vessel.

Pore pressure lines are connected to both the top and the bottom of the sample through holes in the endcaps. When low permeability samples (e.g. shales) are tested, a metal mesh is wrapped around the sample. The pore-fluid lines are in direct contact to the mesh, allowing for side drainage and faster pore pressure equilibration (Figure 2). When the valves in the pore-fluid lines are closed for undrained measurements the dead volume amounts to ~2 ml. For undrained measurements, this is sufficiently small to restrict the drainage effects on the stiffness moduli. Demonstration of drainage effect is shown in Figure 4. Low-frequency measurements have been performed on a saturated sandstone (~30% porosity) with closed and opened valves, respectively. The drainage effect is clearly visible when the valves are open and almost disappears during undrained measurements.

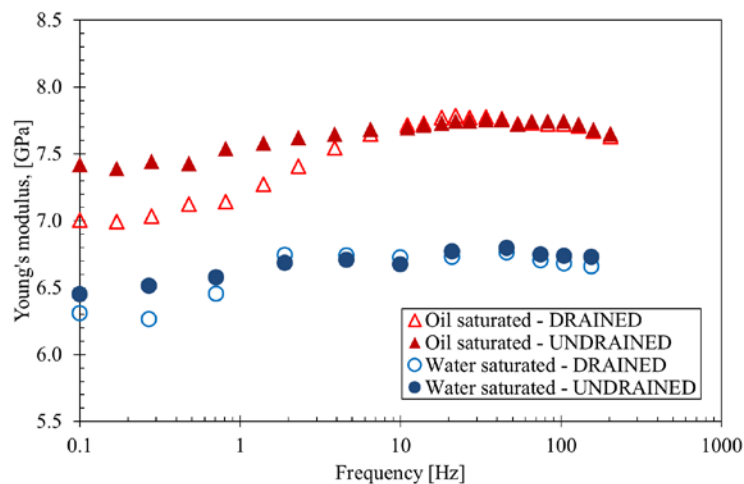


Figure 4. Demonstration of the drainage effect with open (open symbols) and closed (closed symbols) pore pressure valves during the low-frequency measurement with fully water (blue symbols) and oil (red symbols) saturated sandstones. The measurements were done at $\sigma_{\text{ax}} = 10$ MPa, $P_{\text{conf}} = 9$ MPa and $P_t = 2$ MPa.

The strain of the sample is measured by two separate sensor systems shown in Figure 2. The first is represented by three LVDTs (MHR-100) placed around the sample, measuring the axial strain of the sample. The second system is a set of four double resistive strain gages (Vishay CEA-06-125WT-350) for recording local strains in axial and radial directions. These gages are attached to the sample's surface on the middle height, equally distributed around the sample.

B. Uniaxial Stress Low-Frequency Measurements

The principle of this measurement is to apply a small uniaxial stress oscillation of a certain frequency, and record axial and radial strain modulations. In order to convert displacement modulations of a piezoelectric actuator integrated in the sample stack into stress/strain modulations of the sample, a finite deviatoric axial stress (≥ 0.5 MPa) has to be applied to the sample stack during low-frequency measurements. The frequency is limited to about 0.1÷150 Hz range. For elastic measurements strain (rms) amplitudes are usually kept between 10^{-7} ÷ 10^{-6} strain.

As mentioned, for stress modulations, a piezoelectric actuator (PI P-235.1S) is placed in the sample stack inside the triaxial cell (Figure 2). It is controlled by a sinusoidal signal generated in lock-in amplifier (Stanford Research SR850) and amplified by a voltage amplifier (PI E-421). The resulting vertical force modulation is measured by a piezo-electric force sensor (Kistler 9323AA in combination with Kistler 5015A Charge Meter). Amplitude and phase of the force signal is measured by the lock-in amplifier.

The stress-modulation magnitude is calculated from the force amplitude, F , and the cross section of the sample, A :

$$\sigma_{ax} = \frac{F}{A} \quad (1.8)$$

The strain modulations are measured by the same resistive strain gages as for the static measurements. Eight strain gages (four radial and four axial) are connected to four Wheatstone bridges with configuration shown on Figure 5. Signals from active strain gages, R_2 and R_4 , are averaged by the bridge. The input voltage (V_{in}) is 8 V, powered by a laboratory DC power supply.

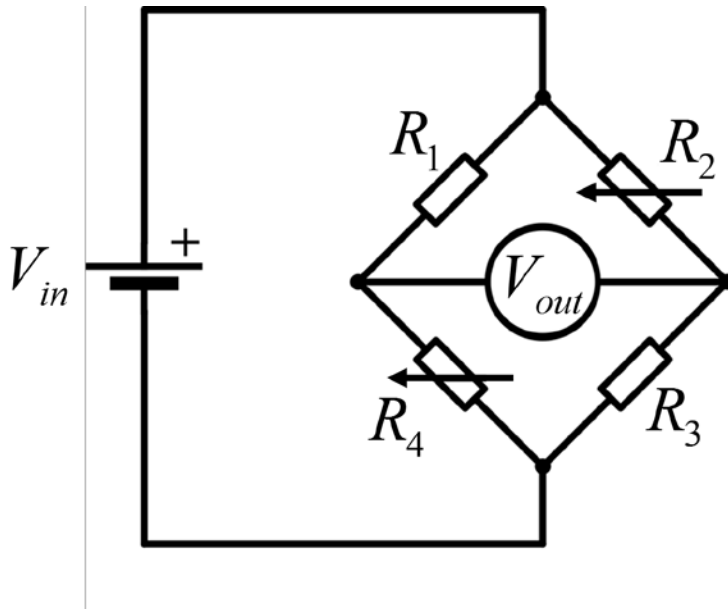


Figure 5. Wheatstone bridge configuration used to acquire the strains of the sample. R_1 and R_3 are passive resistances, R_2 and R_4 represent strain gages attached to the sample's surface from opposite sides. In total, four Wheatstone bridges are used: two for radial and two for axial strains.

Amplitudes and phases of voltage signals from the Wheatstone bridges are measured by four additional lock-in amplifiers (two for axial and two for radial strain signals). Axial and radial strains, ϵ_{ax} and ϵ_r , are calculated by (for configuration shown on Figure 5):

$$\epsilon_{ax,r} = \frac{2R_{ax,r}}{V_{in} \times GF} \quad (1.9)$$

where R_{ax} and R_r are the amplitudes of the measured Wheatstone-bridge voltage signals for the axial and radial strain gauges, respectively, and GF is the gage factor of the strain gages (provided by the manufacturer).

Dynamic Young's modulus and Poisson's ratio are obtained from the stress and strain-modulation amplitudes using Equations (1.1).

The data acquisition for the low-frequency measurements is fully automated. A custom software written in LabVIEW controls the lock-in amplifiers throughout the measurement, acquires and processes the data.

At the beginning of the measurement the user can specify the frequency range and the number of points. Based on calibration measurements, the software will select time constants, acquisitions rates and other parameters for each frequency. Stress and strain amplitudes and phases as well as calculated Young's modulus and Poisson's ratio are displayed in real time. For each frequency, force-sensor and strain-gage signals are recorded at a given rate until all signals are stable within a given error (typically 1-2%).

C. Ultrasonic Frequency Measurements

The conventional pulse-transmission technique (Hughes et al., 1949) is used for measuring ultrasonic P- and S-wave velocity in axial direction. Ultrasonic P- and S-wave transducers and receivers with a central frequency of 500 kHz are mounted inside the titanium endcaps. The velocities are calculated according to:

$$V_{P,S} = \frac{L - \Delta L}{T_{P,S} - T_0} \quad (1.10)$$

where L – is initial length of the sample before the test, ΔL – change of the sample length as a result of applied stresses, $T_{P,S}$ – total wave send-receive travel time, T_0 – system travel time.

The error of the ultrasonic measurements is estimated to be less than 1%. For S-wave velocity, the error may be higher as it is often superposed with strong converted P-wave signal.

Typical recorded P- and S-waveforms with aluminium and shale rock samples are shown on Figure 6.

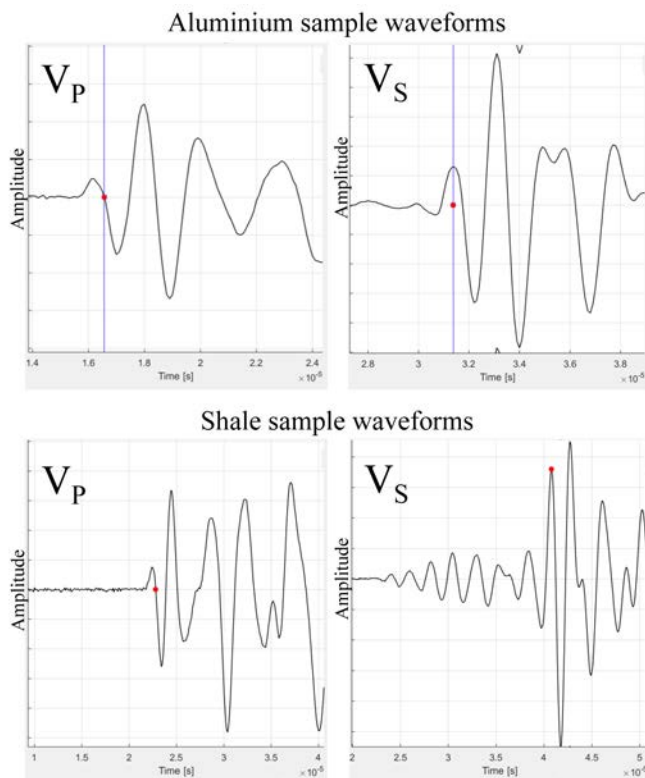


Figure 6. Typical P- and S-waveforms recorded with ultrasonic pulse-transmission technique. Wave arrival pick is shown with red points; P-wave arrival is picked at first zero-crossing, S-wave arrival – at first maximum. Measurements with aluminium sample of known properties (top) are used to calculate system travel time.

III. Errors of the low-frequency measurements

In this section, we will quantify systematic and random errors of the low-frequency measurement. The following approach is used to quantify the uncertainties:

- A) Quantify errors of Young's modulus and Poisson's ratio based on the measurements with aluminium 7075 test sample with known properties.
- B) Quantify errors of velocities based on estimated systematic and random errors of the respective elastic properties.

It should be noted that all results of the low-frequency measurements are presented without any kind of corrections, using factory calibrations for all sensors and equipment, unless otherwise noted.

A. Errors in Young's modulus and Poisson's ratio

Validation tests with an aluminium sample (type 7075) with known properties are performed on a regular basis. Results of those measurements taken over a period of 2 years are presented in Figure 7 (only measurements that are done with the automated acquisition software were included). The measurements were done under different stress conditions: the confining pressure varied from 0 to 20 MPa, and the deviatoric stress from 1.4 to 10 MPa. Aluminium is assumed to be linear elastic and non-dispersive, i.e. its stiffness is stress and frequency independent. The stress oscillation RMS amplitude varied from about 25 to 70 kPa. For the measurements without confining pressure, strain gages were glued to the sample; for the measurements with confining pressure, gages were attached without gluing and were hold in place by confining pressure.

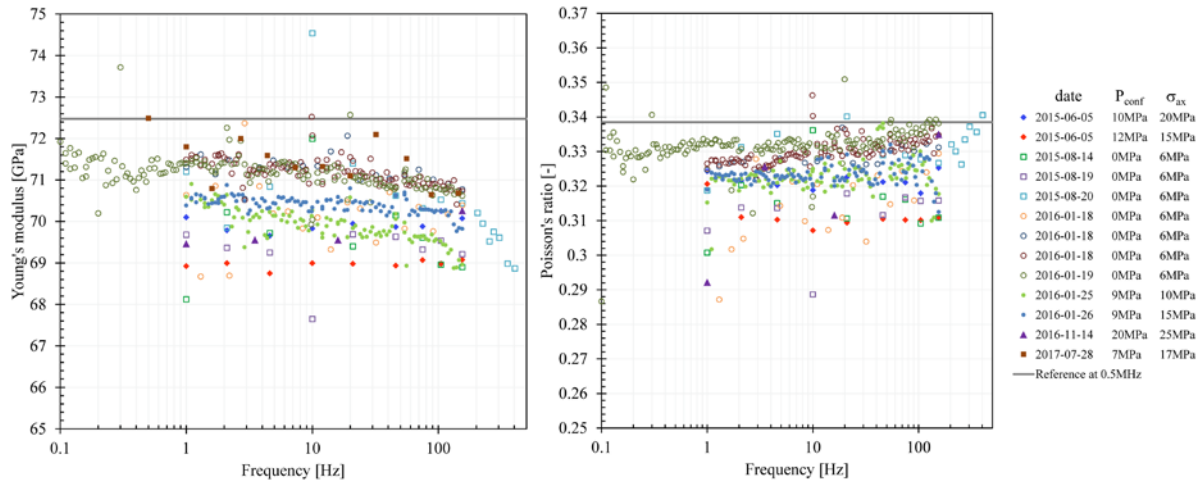


Figure 7. Young's modulus and Poisson's ratio as a function of frequency acquired with an aluminium test sample measured over a period of 2 years under different stress conditions. Reference values at 0.5 MHz were measured on a calibrated ultrasonic setup.

The measured Young moduli and Poisson ratios are slightly lower than the real values. For the different measurements, the systematic error of the measured Young modulus and Poisson ratio (averaged over all frequencies) vary between -4.3% and -1.6%, and between -6.8% and -1.6%, respectively. Random errors were estimated by taking the average of the standard deviation of the measured Young modulus and Poisson ratio for each measurement (each measurement consists of several data points taken at different frequencies). They amount to 0.7% for Young's modulus and 2.3% for Poisson's ratio.

We proceed to a detailed error analysis to investigate the underestimation and spread of the measured stiffness parameters. By combining Eqs. (1.1), (1.8), and (1.9), Young's modulus and Poisson's ratio are given by:

$$E = \frac{R_f FS V_{in} GF}{2A R_{ax}}; \nu = \frac{R_r}{R_{ax}} \quad (1.11)$$

where R_f – is amplitude of the force signal, [V]; FS – force sensor factor, [N/V].

In the following, the systematic and random errors for each parameter in Eq. (1.11) will be discussed, based on results obtained with the aluminium test sample.

It should be noted that the outliers in the experimental data, typically occur around 50 Hz and multiples of 50 Hz, are ignored in the present analysis.

List of systematic errors:

1. Errors of strain measurements (some equations are provided in the appendix):

- a) Angular misalignment of the strain gages relative to the principal strain direction.

Since the gage mounting is a manual operation, we accept a misalignment error of 1° which already becomes visible with a naked eye.

- b) Temperature

The gage factor (strain sensitivity) of the strain gages varies with temperature.

- c) Transverse sensitivity

Transverse sensitivity of strain gages refers to the gage factor change as response to strains which are perpendicular to the direction of the measured strain.

- d) Confining pressure

The confining pressure that acts on the strain gages may induce cross-section changes and, as result, resistance changes. This effect has been studied and considered negligible.

- e) Wheatstone bridge input-voltage error

Error of the laboratory DC power supply voltage output .

- f) Possible slip of unglued strain gages is assumed to result in less than 1% error in strain (the subject was studied by Szewczyk et al. (2016) and Lozovyi et al., (2017); see also comment in item 5).

2. Errors of stress measurements:

- a) The force sensor is temperature sensitive;
- b) Error of the charge meter used in combination with the force sensor;
- c) Force sensor sensitivity dependence on confining pressure has not been specifically studied, but there are no indications for any significant effect;
- d) Error in measuring cross-section area of the sample.

3. Sample misalignment:

An increase in axial deviatoric stress was observed to lead to an apparent increase in Young's modulus in measurements with aluminium. It can possibly be explained by an uneven stress distribution if the sample is slightly tilted with respect to the applied axial stress, resulting in an apparently smaller Young modulus. A better alignment enforced by higher axial stresses results in a more even stress distribution and a reduced error in Young's modulus. The error in Young's modulus and Poisson's ratio due to sample misalignment are up to about -1.5 % and -2 %, respectively. Stresses are much better redistributed in more compliant rock samples where such errors are not expected.

4. Sample bulging:

When the vertical load is applied to the rock sample in a triaxial cell, friction develops on the interfaces between sample's surfaces and pistons. The friction doesn't allow the sample around the boundaries to expand (as result of Poisson's effect). This leads to a local stiffening of the sample and bulging. From rock mechanical testing, it has been shown that length/diameter ratio should of at least

2 so that the sample could be sufficiently long to accommodate a shear plane penetrating through the side walls (Fjær et al., 2008).

5. Friction between rubber jacket and oil:

A detailed study has not been performed yet. We observe an about 1% difference in Young's modulus in tests with and without confining pressure (and oil). However, this difference may also be due to better sample alignment and more homogeneous stress distribution in the sample if confining pressure is applied (as discussed above), or it could be related to strain gage slippage since the measurements with and without confining pressure were performed with non-glued and glued gages, respectively.

Systematic error sources for the aluminium testing that are possible to quantify are summarized in Table 1. For calculation of temperature-induced errors, temperature range from 20 to 24°C was used.

Table 1. Systematic errors in aluminium testing

Parameter	Stress			Strain			
	Force amplitude, R_f	Force sensor factor, FS	Sample cross-section, A	Amplitude of the axial strain signal, R_{ax}	Amplitude of the radial strain signal, R_r	Bridge input voltage, V_{in}	Gage factor, GF
Typical value	0.67 V	20 N/V	507 mm ²	8 μ V	2.7 μ V	8 V	2.17
Error [%]	± 3	$-0.2 \div 0$	$-0.5 \div 0.08$	$-0.09 \div -0.02$	$-2.6 \div -1.5$	± 0.7	$-0.06 \div 0$

Using the systematic error boundaries from Table 1 for each of the constituents in Eq. (1.11), we can calculate errors in Young's modulus and Poisson's ratio (Table 2).

Table 2. Theoretically predicted systematic error boundaries for Young's modulus and Poisson's ratio in aluminium testing.

Young's modulus error, [%]	$-4 \div +4$
Poisson's ratio error, [%]	$-2.5 \div -1.5$

The error in Young's modulus seems to be mostly due to sample misalignment (item 3) and a relatively large error in the force measurement (item 2a). Underestimation of Poisson's ratio is partially caused by transverse sensitivity of the strain gages (item 1c). The effect is larger for radial-strain measurements than for axial-strain measurements since the radial gages are sensing a part of the significantly larger axial strains (see appendix). As a result, the radial strain is underestimated more than the axial strain which leads altogether to an underestimation of Poisson's ratio. Transverse sensitivity does not fully explain the measured lower bound of the error in Poisson's ratio. Another systematic error source may be an error in strain amplitude produced by lock-in amplifiers. Yet this effect is hard to quantify. Random errors in Young's modulus correlate with random errors in axial strain amplitude (R_{ax}). Random errors in Poisson's ratio are mostly related to random errors in radial-strain amplitude (R_r).

For measurements with rock samples, additional error sources have to be considered. On the other hand, rocks and especially shales are more compliant than aluminium. That results in a better sample alignment and a reduced error due more homogeneous stress distribution. We estimate errors of the low-frequency measurement with rocks on the example Opalinus Clay that has been reported as a highly homogeneous rock (Jaeggi et al., 2017). Three fully saturated aliquot samples from the shaly facies of Opalinus Clay were tested under identical conditions. Axial stress, confining pressure, and pore pressure were 7.5 MPa, 7 MPa, and 3 MPa, respectively. Figure 8 shows the results for measured Young's modulus and Poisson's ratio. Since the samples were cored within a distance of a few centimetres, it is assumed that the tested core plugs have the same mechanical properties and that the differences in the measured stiffnesses are mostly due to measurement errors. For the three tests, Young's modulus and

Poisson's ratio averaged over the frequency range of 1–144 Hz vary by 4% and 2.5%, respectively.

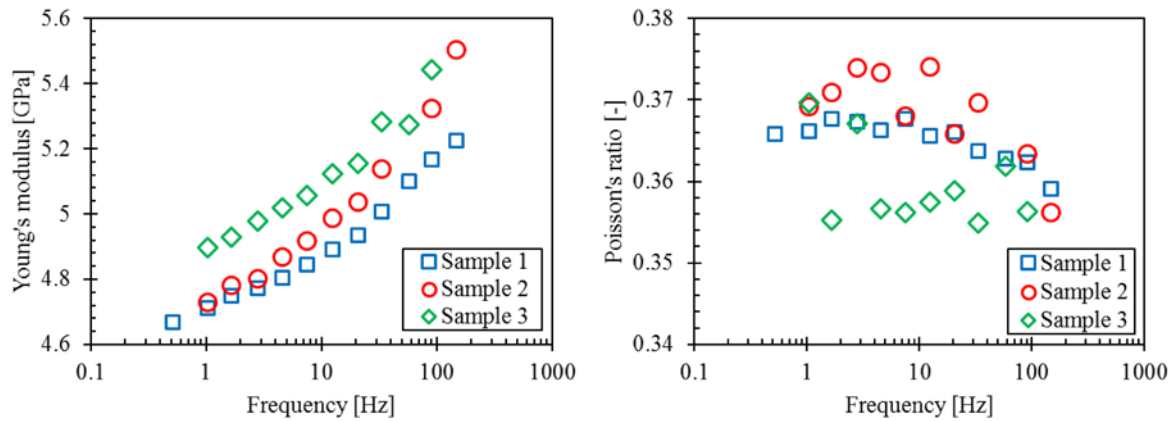


Figure 8. Results of the tests performed with three homogeneous samples of Opalinus Clay shale from the same depth and at the same stress state to give an estimate of systematic error of the low-frequency measurement with rock samples.

In addition to the error sources identified for the aluminium sample, next errors of the low-frequency measurements are relevant for rock samples:

1. Heterogeneities of the sample

Since the strain is measured locally on an area of about 10 mm², the measured strain may not be representative for the average strain of the sample dependent on the degree of stiffness heterogeneity and the length scale over which stiffness variations occur. Such errors are rock specific and difficult to estimate.

2. Stress measurement errors

Initial cross-sectional area of the sample is used to calculate the axial stress. It is assumed to be unchanged when the static stress is applied. Since the rocks are usually more compliant than aluminium, changes in cross-sectional area of the sample are regarded as an error source (much less than 1%).

Additional error sources in measurements with TI rocks (e.g. shales):

3. Strain gage orientation errors

Circumferential misplacement of strain gages relative to the sample axis on 90° oriented samples as it has two radial principal strain directions. A ±2° shift will result in Poisson's ratio errors ν_{HV} : -1 ÷ 0%, ν_{HH} : 0 ÷ 2% (assuming a linear angle dependence of Poisson's ratio).

Errors that are less prominent with rocks than with aluminium:

1. Insufficient static axial deviatoric stress

Rocks, especially shales, require less deviatoric force to close the interfaces and redistribute stresses in case of a tilt of the sample axis;

2. Slip of the strain gages

The surface of a rock is rougher than that of aluminium, therefore it is less likely that the non-glued gages slip.

Table 3 lists errors in Young's modulus and Poisson's ratio for the rock sample testing. We take errors in stiffness for aluminium as a reference error (only from the measurements where the sufficient axial stress was applied, as we consider equal stress distribution in rock samples). Strain gage orientation errors for TI samples (item 3) are added to the uncertainties for aluminium to quantify errors for 90° oriented sample.

Table 3. Systematic and random errors in low-frequency rock sample testing with uniaxial stress conditions.

	Isotropic sample (0° for TI)		90° sample			45° sample
	E (E _V)	ν (ν_{VH})	E _H	ν_{HH}	ν_{HV}	E ₄₅
Typical value	5 GPa	0.33	7.6 GPa	0.25	0.5	6.2 GPa
Systematic error, [%]	-4.0 ÷ -1.2	-4.8 ÷ -2.5	-3.9 ÷ -1.2	-6.4 ÷ -4.7	-3.8 ÷ -2.0	-4.0 ÷ -1.2

Random error, [%]	±0.7	±2.3	±0.7	±2.3	±2.3	±0.7
-------------------	------	------	------	------	------	------

B. Errors in velocities

Another error source in the determination of seismic velocities from dynamic rock-stiffness measurements is the error in rock density. The rock density is obtained from length and diameter, and the weight of the sample; typical values and their errors are given in Table 4. Here, we account for errors in the initial weight and sample dimensions as well as stress induced changes for a material with a stiffness as given in Table 3 tested at confining pressures up to 15 MPa (it is also assumed that fully saturated shales may swell under insufficient stress conditions (Ewy, 2015)).

Table 4. Error in samples density for accounting in velocity error calculation.

	Length	Weight	Cross section area, A	Density, ρ
Typical value	5.08 cm	65 g	5.07 cm ²	2.5 g/cm ³
Error, [%]	-0.2÷0.3	-0.25÷0.24	-0.5÷0.9	-0.5÷1.0

Isotropic rocks

For isotropic rocks, two measured independent stiffness parameters (Young's modulus, E, and Poisson's ratio, ν) together with the density, ρ , are used to calculate P- and S-wave velocities as shown in Eq. (1.2). The total differentials of V_P and V_S are used to calculate the velocity errors from errors in dynamic Young's modulus, Poisson's ratio, and density:

$$\Delta V_P = \frac{1-\nu}{2\sqrt{E\rho(1-\nu^2)(1-2\nu)}} \Delta E + \sqrt{\frac{E\nu^2(2-\nu)^2}{\rho(1-2\nu)^3(1+\nu)^3(1-\nu)}} \Delta \nu - \sqrt{\frac{E(1-\nu)}{4\rho^{4/3}(1-2\nu)(1+\nu)}} \Delta \rho$$

$$\Delta V_S = \frac{1}{2\sqrt{2E\rho(1+\nu)}} \Delta E - \frac{E}{2\sqrt{2E\rho(1+\nu)^3}} \Delta \nu - \frac{E}{2\sqrt{2E\rho^3(1+\nu)}} \Delta \rho$$

(1.12)

Using these relations and estimated errors of Young's modulus, Poisson's ratio (Table 3) and density (Table 4), errors in V_p and V_s are calculated (see Table 5).

Transverse isotropic (TI) rocks

In addition to measurement errors listed in Table 3 for Young's moduli and Poisson's ratios, the following error sources have to be considered in velocity calculations for transversely isotropic rocks:

1. Error in sample orientation when drilling core plugs.

In error calculations, we assume a maximum deviation of 5° for each sample orientation. The change in Young's moduli and Poisson's ratios for 0° and 90° samples (deviated to 5° and 85° respectively) is between -0.1 to 0.3 %. However, the largest error would be for 45° sample. If deviated to 40° or 50° the error in E_{45} modulus is up to 1%.

2. Deviations from TI symmetry.

Shales may also exhibit anisotropy within the bedding plane (e.g. induced by stresses), hence they may have a lower symmetry than TI symmetry assumed in our calculations. Errors due to a reduced symmetry are hard to estimate unless the symmetry of the rock is well characterized.

3. Errors associated with deviatoric stresses applied in low-frequency measurement:

Measurements with differently oriented non-isotropic samples should be carried out under identical stress conditions, which, in a biaxial cell, is only possible for hydrostatic stresses. However, with the present setup, low-frequency measurements require a small deviatoric stress (discussed

in Chap. II b) that affects the rock stiffness and results in errors in the calculated velocities. For Opalinus Clay, we have observed an increase in Young's modulus of 2% by increasing the deviatoric stress from 1 MPa to 2 MPa. Most of the measurements in the low-frequency apparatus are done at 1 MPa deviatoric stress so we assume an error in Young's modulus of -2% due to the presence of deviatoric stresses. No change in Poisson's ratio was observed with change in deviatoric stress. Obviously different shales will exhibit different stress sensitivities, so this error will depend on rock type and stress state.

For measurements with Opalinus Clay (three different sample orientations; uniaxial stress oscillation tests), seismic velocities were derived and an error analysis was carried out, taking into account the quantifiable errors listed above. P- and S-wave velocities perpendicular and parallel to bedding, together with estimates of systematic and statistical errors are listed in Table 5. For the vertical P-wave velocity, V_{P0} , the error analysis indicates that the calculated value is most likely smaller than the real velocity by approximately 5% (the systematic error was estimated to be in the range between -1% and -9%). The estimated error does not include contributions due to rock heterogeneity or deviations from TI symmetry, which means that the total error may be even larger, possibly exceeding 10%, which makes it difficult to compare the seismic velocities obtained from low-frequency measurements with ultrasonic velocities and determine the degree of dispersion (note that ultrasonic velocities are directly measured with an error of less than 1%).

Table 5. Measurement errors in the velocities for isotropic and transversely isotropic rock testing in the low-frequency setup (uniaxial stress oscillation test).

	Isotropic sample	Set of transversely isotropic samples
--	------------------	---------------------------------------

	V _P	V _S	V _{P0}	V _{S0}	V _{P90}	V _{S90}
Typical value	1710 m/s	860 m/s	1880 m/s	940 m/s	2180 m/s	1100 m/s
Systematic error, [%]	-5.4 ÷ -1.9	-1.9 ÷ 0	-9 ÷ -1	-5.5 ÷ 2.5	-8 ÷ -1.5	-3 ÷ 0.5
Random error, [%]	±1.7	±0.1	±1	±0.5	±1.5	±0.2

IV. Direct P-wave modulus measurement technique at low frequency

As demonstrated in this work, for anisotropic rocks, the determination of seismic velocities based on low-frequency measurements with three differently oriented samples results in significant errors that may even exceed 10% if the rocks are heterogeneous. The errors connected with heterogeneities and mounting aspects of differently oriented samples can be significantly reduced if P- or S-wave moduli could directly be measured with a single sample. Here, we present a method for measuring the P-wave modulus, C_{33} by applying a uniaxial-strain modulation instead of a uniaxial stress modulation.

A. Description of the system

The principle of the technique is to completely restrict the radial strain of the 0° sample during axial force oscillations and record stress and strain as described in chapter 1. Such uniaxial-strain (oedometric) conditions would allow to calculate the dynamic P-wave modulus according to Eq. (1.7). Uniaxial-strain conditions were achieved by oscillating the radial stress in the pressure vessel. The radial oscillation was adjusted in amplitude and phase relative to the axial modulation in such a way that $\epsilon_{\text{rad}} = 0$ as it is shown on Figure 9. The confining pressure was modulated by means of a custom-built hydraulic actuator, a stepper-motor driven hydraulic cylinder connected to the pressure vessel (paraffin was used as confining fluid).

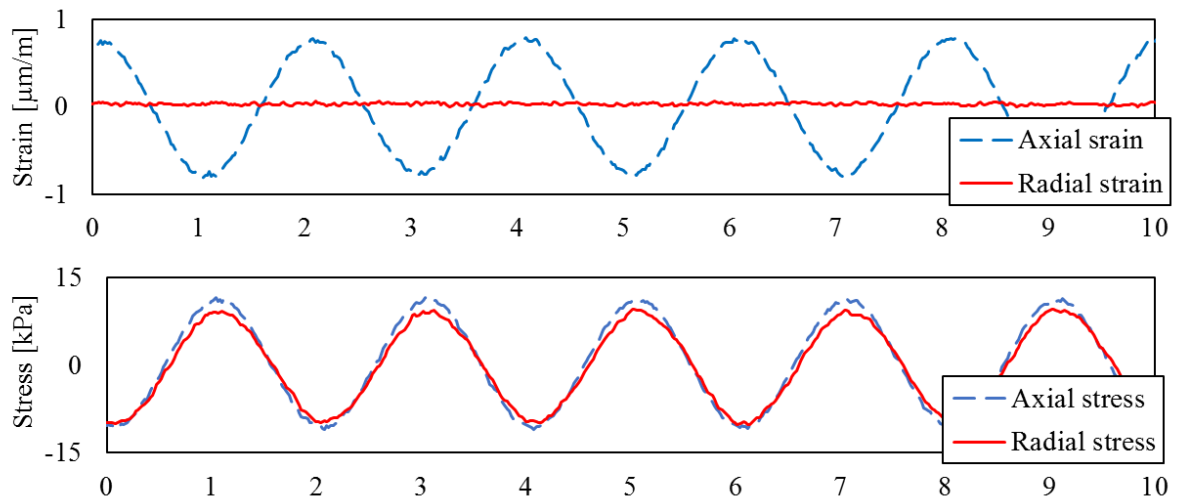


Figure 9. Stress and strain signals recorded during direct P-wave modulus measurement at 0.5 Hz with Opalinus Clay shale.

The hydraulic actuator meets the following requirements: (i) generate smooth sinusoidal pressure oscillations resulting in sample strains of the order of 10^{-6} at the frequency of at least 1 Hz, (ii) operate at confining pressure of at least 20 MPa, and (iii) provide position feedback control.

The hydraulic cylinder contains a piston with a diameter of 3 mm and a maximum stroke of 50 mm, allowing for a volume change of up to 0.4 ml. As a driver, we use a commercial linear actuator (Oriental Motor EAC6-E05-ARAC-3) with a minimum step length of 0.006 mm. The maximum velocity is 300 mm/s that allows to operate the hydraulic cylinder at 1 Hz with maximum amplitude, or at 7 Hz at a quarter of the maximum amplitude, which is sufficient for most applications. The motor thrust of 400 N is enough to operate at pressures up to 50 MPa. As a sealing, two pairs of NBR O-rings are used, one pair is installed on the piston head and another in a gland bushing at the back of the cylinder. Teflon guiding rings are used for centering the piston. The cylinder has been tested at pressures up to 20 MPa.

The setup is shown in Figure 10. The hydraulic cylinder (E) is connected to the pressure cell (A) with a short (~50 cm) steel tube (C) with an inner diameter of 3 mm to eliminate fluid friction effects. A ball valve (D) is inserted in the tube connection for safety. To control the motor, we use own software that is operated from a PC (K). Commands are sent to the motor controller (H) via USB. The controller is connected to a pulse input driver (G) which directly controls the stepper motor (F) and maintains precise positioning through a position feedback control.

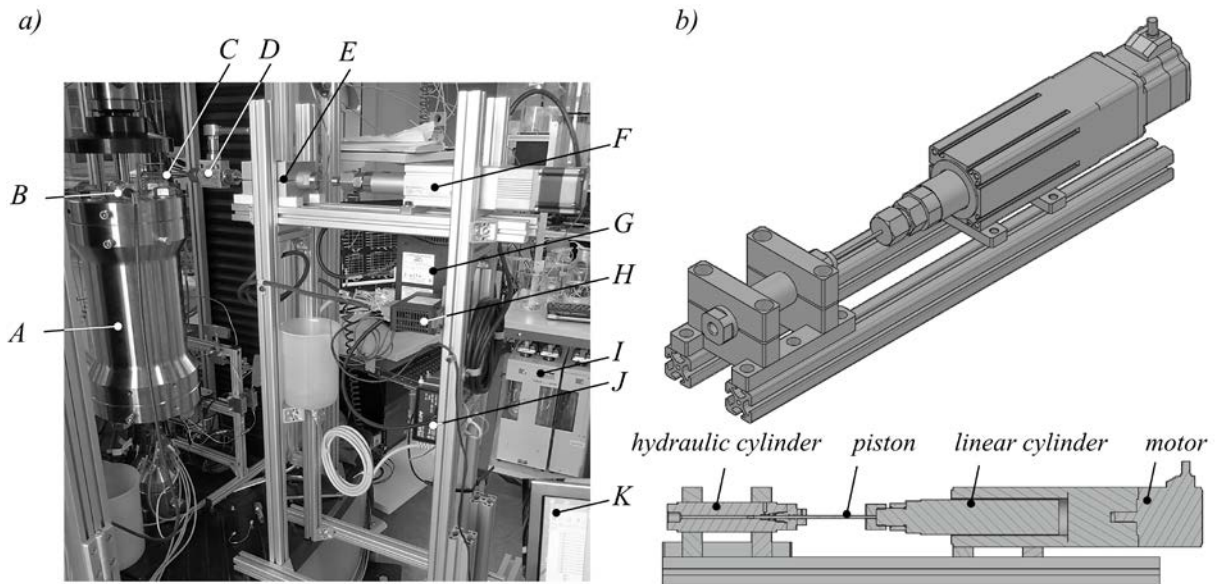


Figure 10. a) Photograph of the low-frequency apparatus with connected module for direct P-wave modulus measurements: A - pressure cell; B - confining pressure gage; C - steel tubing that connects hydraulic cylinder to a pressure cell; D – ball valve; E – hydraulic cylinder; F – linear actuator; G – motor driver; H – motor controller; I – static confining pressure pump; J – controller power supply; K – computer that controls the motor. b) Schematic drawings of the hydraulic cylinder with linear actuator module.

The software that controls the cylinder operation is written in LabVIEW. It allows for real-time amplitude, frequency and offset control.

The control works reliably for frequencies of up to 4 Hz, but the best results in suppressing the radial strain are achieved at sub-hertz frequencies.

B. Operation and data handling

In order to suppress the radial strain for direct P-wave modulus measurements we use the following procedure:

- 1) Oscillate the axial stress only, adjust the amplitude so axial strain amplitude to be $\sim 1 \times 10^{-6}$ and measure the radial strain amplitude;
- 2) Oscillate the confining stress only and adjust the amplitude so that the radial strain amplitude is the same as in step 1;
- 3) Turn both axial and radial stress oscillations. Using the software that controls the cylinder operation adjust the phase of the radial strain oscillations until the radial strain is completely suppressed as shown on Figure 9;
- 4) Record stress and strain signals.

Currently these steps are performed manually, but it is planned to automate them.

Stress and strain signals are acquired with HBM QuantumX MX840 amplifier and Catman DAQ Software. The strain signals are conditioned at frequencies of 1-5 kHz. The advantage of this method over lock-in amplifiers is the ability to observe and analyse the signal in real time. The modulation amplitudes of the axial-force-sensor signal, the confining pressure, and the axial strain are obtained from Fourier transforms of the recorded stress and strain signals.

Since the sample and the axial-force sensor have different cross-sectional areas, a change in confining pressure will result in different forces acting on the force sensor and the sample, which needs to be corrected for (in comparison, the mechanical force induced by the piezo-electric displacement actuator is the same for force sensor and sample). A calibration

measurement is performed in the following way in order to find the (effective) cross-sectional area of the force sensor:

Confining pressure oscillations are performed with the upper piston retracted (hydrostatic stress only, see Figure 11a). The cross-sectional area of the force sensor, A_{sensor} , is given by the ration between axial-force and confining-pressure amplitudes:

$$A_{\text{sensor}} = F / P_{\text{conf}} \quad (1.13)$$

In the general case, with the piston exerting an axial force onto the sample, and knowing the sensor area, the total axial force acting on the sample, F_{sample} , can be calculated from the recorded force measured by the force-sensor, F_{sensor} , in the following way (see Figure 11b):

$$\begin{aligned} F_{\text{sample}} &= F_{\text{sensor}} + F_{\text{corr}} \\ F_{\text{corr}} &= P_{\text{conf}} \cdot (A_{\text{sample}} - A_{\text{sensor}}) \end{aligned} \quad (1.14)$$

Under uniaxial strain conditions (zero radial strain), the P-wave modulus, C_{33} , is then given by:

$$C_{33} = F_{\text{sample}} / A_{\text{sample}} / \varepsilon_{\text{ax}} \quad (1.15)$$

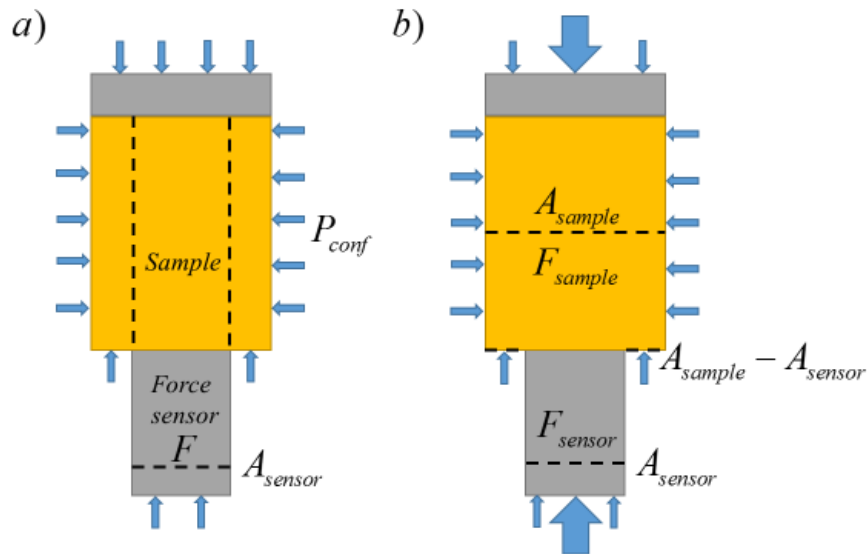


Figure 11. Illustration of full force estimation during direct P-wave modulus measurement.

C. Validation and test results

A validation measurement has been done on an aluminium sample (non-dispersive, isotropic, and homogeneous material). The P-wave velocity of the reference sample measured at ultrasonic frequencies (500 kHz) amounts to 6288 m/s, corresponding to a P-wave modulus of 110.9 MPa. Using the method of direct P-wave modulus measurements at a frequency of 0.5 Hz, we obtained a P-wave modulus of 104.6 GPa, and $V_P = 6105$ m/s (Figure 12). Under the assumption that the velocities and moduli are frequency independent, and given that the ultrasonic velocity has a small error ($< 1\%$), the error of the low-frequency P-wave velocity and P-wave modulus are -3% and -6% , respectively. For an isotropic material such as aluminium, the P-wave velocity could also be determined with a similar error by performing conventional low-frequency measurements under uniaxial-stress conditions (measurement of Young's modulus and Poisson's ratio; see Figure 12). However, for TI-symmetry media such as shales, an error of 3% in the P-wave velocity, V_{P0} , is a significant improvement compared to conventional low-frequency measurements with differently oriented samples. The error in

velocity, V_{P0} , determined from the measurements with three differently oriented core plugs can be up to about -10% (see Table 5) and even more if the rock is heterogeneous.

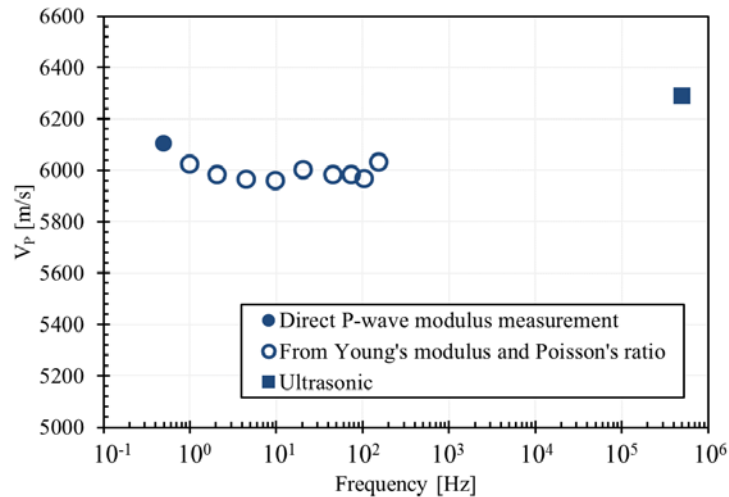


Figure 12. Velocity as a function of frequency in validation measurements with aluminium sample. Velocity at 0.5 Hz derived from the direct P-wave modulus measurement is shown in closed circle; Velocities at 1- 155 Hz derived from the conventional Young's modulus and Poisson's ratio measurement are shown in open circles; Reference measurement at ultrasonic frequency is shown in square.

First rock measurements, using the new technique, have been performed with Opalinus Clay (shaly facies). First, using two different sets of 0° , 45° and 90° oriented samples, P-wave velocities were obtained by applying the conventional low-frequency technique in the frequency range 1-144 Hz. In addition, the new technique was applied with the 0° -oriented samples at a frequency of 0.5 Hz. Ultrasonic velocities are measured at 500 kHz. The measured vertical P-wave velocities, V_{P0} , as a function of frequency are shown in Figure 13. Note that Set 1 has been tested at two different net stresses ($P_{\text{conf}}' = P_{\text{conf}} - P_f$). At a lower net stress (L) next stress conditions were applied: $P_{\text{conf}} = 7$ MPa, $P_f = 3$ MPa; and at higher stress state (H): $P_{\text{conf}} = 13$ MPa, $P_f = 3$ MPa. Set 2 has been only tested at lower net stress.

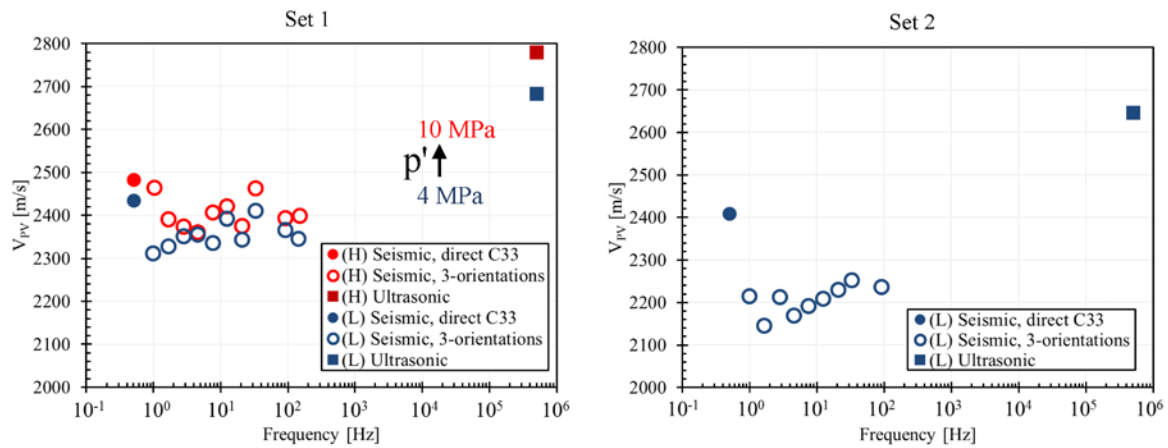


Figure 13. Vertical P-wave velocity as a function of frequency measured for two sets of Opalinus Clay samples. Measurement results of the new direct P-wave modulus technique at 0.5 Hz (closed circles) are compared to conventional low-frequency (open circle) and ultrasonic measurements (squares). Set 1 was tested at lower (L) and higher (H) net stresses ($P_{conf}' = P_{conf} - P_t$) of 4 MPa and 10 MPa, respectively. Pore pressure was kept 3 MPa for all the measurements.

The results show that velocities measured with the conventional low-frequency technique are significantly smaller than those obtained from direct P-wave modulus measurements that are considered more accurate. Note that the velocities obtained from direct P-wave modulus measurements are consistent with the ultrasonic velocities; for both samples a dispersion of around 200 m/s is observed between seismic and ultrasonic frequencies, with the velocity of the 0° -sample from Set 1 being slightly higher than that of the 0° -sample from Set 2. For Set 1, the velocity at 1 Hz obtained by the conventional low-frequency technique is 5% lower than that obtained with the direct P-wave modulus technique (at 0.5 Hz); for Set 2 this difference is 9%. These errors are within the range of estimated errors of conventional low-frequency measurements (see Table 5). The example on Opalinus Clay shows that conventional low-frequency measurements may greatly overestimate the dispersion of velocities by up to a 100%. For anisotropic rocks, it is therefore recommended to perform direct P-wave modulus measurements. Since it is difficult to perform such measurements at higher frequencies, the

direct P-wave modulus measurements at 0.5 – 1 Hz can be used to calibrate the velocity data obtained from conventional low-frequency measurements at 1-150 Hz.

V. Conclusion

Dynamic stiffness measurements at seismic frequencies in combination with ultrasonic measurements inside a triaxial cell provide a valuable information on seismic dispersion in fluid-saturated rocks. However, for anisotropic rocks such as shales, large errors in seismic velocities of up to 10% or more may arise when low-frequency measurements are carried out under uniaxial-stress conditions (conventional low-frequency technique), and seismic velocities are determined from Young's modulus and Poisson's ratio measurements with differently oriented samples. Such large errors make it difficult to determine the dispersion of velocities between seismic and ultrasonic frequencies, as for shales, the dispersion is typically on the order of 10%. In this work, we demonstrate that it is possible to directly measure the P-wave modulus of a sample at seismic frequencies by synchronized axial-force and confining-pressure modulations. In this way, P-wave velocities can be obtained from low-frequency measurements with one sample only, and the velocity errors are reduced to approximately 3%.

Acknowledgments

The authors acknowledge financial support from The Research Council of Norway (Grant no. 234074/E30), AkerBP, DONG Energy, ENGIE, Maersk and Total through the PETROMAKS 2 KPN-project: Shale Rock Physics: Improved seismic monitoring for increased recovery at SINTEF. The authors also acknowledge two anonymous reviewers for their constructive comments and suggestions that have improved this paper.

Appendix – error calculations in strain gage measurements

A. Angular misalignment of the strain gages

Absolute strain error (ε') due to angular misalignment of the strain gages from principal strain axis is calculated using equation (Micro Measurements, 2014a):

$$\varepsilon' = \frac{\varepsilon_v - \varepsilon_h}{2} (\cos 2\phi - 1) \quad (A1)$$

where ε_v and ε_h are vertical and horizontal strains in principal directions, ϕ is angle between direction of the measurement and principal strain direction. For a material with Poisson's ratio of ~ 0.3 the error in axial strain is $-0.04\% \div 0\%$ and $-0.12\% \div 0\%$ in radial.

B. Temperature

The alloys used in resistance strain gages typically exhibit a change in gage factor with temperature. The dependence is linear and corrected gage factor calculated as follow (Micro Measurements, 2014b):

$$GF = GF_{nom.} \left(1 + \frac{\Delta F(\%)}{100} (t - t_{nom.}) \right) \quad (A2)$$

where GF found for given temperature t , $GF_{nom.}$ is a nominal gage factor at the temperature $t_{nom.}$, ΔF is a temperature compensation factor.

C. Errors due to transverse sensitivity in strain gages

Transverse sensitivity in a strain gage refers to the behaviour of the gage in responding to strains which are perpendicular to the primary sensing axis of the gage. The correct strains along any two perpendicular axes can always be calculated from the following equations in terms of the indicated strains along those axes (Micro Measurements, 2011):

$$\begin{aligned}\varepsilon_v &= \frac{(1 - \nu_0 K_t)(\hat{\varepsilon}_v - K_t \hat{\varepsilon}_h)}{1 - K_t^2} \\ \varepsilon_h &= \frac{(1 - \nu_0 K_t)(\hat{\varepsilon}_h - K_t \hat{\varepsilon}_v)}{1 - K_t^2}\end{aligned}\tag{A3}$$

where ε_v and ε_h are actual vertical and horizontal strains, $\hat{\varepsilon}_v$ and $\hat{\varepsilon}_h$ are measured strains, ν_0 – the Poisson's ratio of the material on which the manufacturer's gage factor, was measured (usually 0.285), K_t – transverse sensitivity coefficient.

References

- Batzle, M.L., Han, D.-H., and Hofmann, R. (2006). Fluid mobility and frequency-dependent seismic velocity — Direct measurements. *GEOPHYSICS* 71, N1–N9.
- Bower, A.F. (2010). *Applied mechanics of solids* (Boca Raton: CRC Press).
- Duranti, L., Ewy, R., and Hofmann, R. (2005). Dispersive and attenuative nature of shales: multiscale and multifrequency observations. In *75th Annual International Meeting, (Society of Exploration Geophysicists)*, pp. 1577–1580.
- Ewy, R.T. (2015). Shale/claystone response to air and liquid exposure, and implications for handling, sampling and testing. *Int. J. Rock Mech. Min. Sci.* 80, 388–401.
- Fjær, E., Holt, R.M., Horsrud, P., Raaen, A.M., and Risnes, R. (2008). *Petroleum Related Rock Mechanics* (Elsevier).
- Fjær, E., Holt, R.M., Nes, O.M., Stenebraten, J.F., and others (2011). The transition from elastic to non-elastic behavior. In *45th US Rock Mechanics/Geomechanics Symposium, (American Rock Mechanics Association)*, p.
- Getting, I.C., Paffenholz, J., and Spetzler, H.A. (1990). Measuring Attenuation in Geologic Materials at Seismic Frequencies and Amplitudes. In *The Brittle-Ductile Transition in Rocks*, A.G. Duba, W.B. Durham, J.W. Handin, and H.F. Wang, eds. (American Geophysical Union), pp. 239–243.
- Hatchell, P., and Bourne, S. (2005). Rocks under strain: Strain-induced time-lapse time shifts are observed for depleting reservoirs. *Lead. Edge*.
- Holt, R.M., Fjaer, E., Bauer, A., and others (2013). Static and Dynamic Moduli—so Equal, and yet so Different. In *47th US Rock Mechanics/Geomechanics Symposium, (American Rock Mechanics Association)*, p.
- Hughes, D.S., Pondrom, W.L., and Mims, R.L. (1949). Transmission of Elastic Pulses in Metal Rods. *Phys. Rev.* 75, 1552–1556.

Jackson, I., Paterson, M.S., Niesler, H., and Waterford, R.M. (1984). Rock anelasticity measurements at high pressure, low strain amplitude and seismic frequency. *Geophys. Res. Lett.* *11*, 1235–1238.

Jaeggi, D., Bossart, P., and Nussbaum, C. (2017). The Rock Mechanical Behavior of Opalinus Clay – 20 Years of Experience in the Mont Terri Rock Laboratory. In *Advances in Laboratory Testing and Modelling of Soils and Shales (ATMSS)*, (Springer, Cham), pp. 351–356.

Lozovyi, S., Sirevaag, T., Szewczyk, D., Bauer, A., and Fjær, E. (2017). Non-Elastic Effects in Static and Dynamic Rock Stiffness. In *Proceedings of the 51th US Rock Mechanics Symposium - ARMA*, (American Rock Mechanics Association), p.

Mavko, G., Mukerji, T., and Dvorkin, J. (2009). *The rock physics handbook. Tools for seismic analysis of porous media* (Cambridge, UK ; New York: Cambridge University Press).

Micro Measurements (2011). *Errors Due to Transverse Sensitivity in Strain Gages*.

Micro Measurements (2014a). *Strain Gage Rosettes: Selection, Application and Data Reduction*.

Micro Measurements (2014b). *Strain Gage Thermal Output and Gage Factor Variation with Temperature*.

Mikhailtsevitch, V., Lebedev, M., and Gurevich, B. (2014). Measurements of the elastic and anelastic properties of sandstone flooded with supercritical CO₂. *Geophys. Prospect.* *62*, 1266–1277.

Murphy, W.F. (1982). Effects of partial water saturation on attenuation in Massillon sandstone and Vycor porous glass. *J. Acoust. Soc. Am.* *71*, 1458–1468.

Nye, J.F. (1984). *Physical properties of crystals: their representation by tensors and matrices* (Oxford [Oxfordshire] : New York: Clarendon Press ; Oxford University Press).

Pimienta, L., Fortin, J., and Guéguen, Y. (2015). Bulk modulus dispersion and attenuation in sandstones. *GEOPHYSICS* *80*, D111–D127.

Røste, T., Landrø, M., and Hatchell, P. (2007). Monitoring overburden layer changes and fault movements from time-lapse seismic data on the Valhall Field. *Geophys. J. Int.* *170*, 1100–1118.

Sayers, C.M. (2005). Seismic anisotropy of shales. *Geophys. Prospect.* *53*, 667–676.

Sayers, C.M. (2012). The effect of anisotropy on the Young's moduli and Poisson's ratios of shales. *Geophys. Prospect.* *61*, 416–426.

Spencer, J.W. (1981). Stress relaxations at low frequencies in fluid-saturated rocks: Attenuation and modulus dispersion. *J. Geophys. Res.* *86*, 1803–1812.

Subramanian, S., Quintal, B., Tisato, N., Saenger, E.H., and Madonna, C. (2014). An overview of laboratory apparatuses to measure seismic attenuation in reservoir rocks: Apparatuses to measure seismic attenuation. *Geophys. Prospect.* *62*, 1211–1223.

Szewczyk, D., Bauer, A., and Holt, R.M. (2016). A new laboratory apparatus for the measurement of seismic dispersion under deviatoric stress conditions. *Geophys. Prospect.* 64, 789–798.

Szewczyk, D., Bauer, A., and Holt, R.M. (2017). Stress-dependent elastic properties of shales—laboratory experiments at seismic and ultrasonic frequencies. *Geophys. J. Int.* 212, 189–210.

Szewczyk, D., Holt, R.M., and Bauer, A. (2018). The impact of saturation on seismic dispersion in shales — Laboratory measurements. *GEOPHYSICS* 83, MR15–MR34.

Tisato, N., and Madonna, C. (2012). Attenuation at low seismic frequencies in partially saturated rocks: Measurements and description of a new apparatus. *J. Appl. Geophys.* 86, 44–53.

Winkler, K., and Nur, A. (1979). Pore fluids and seismic attenuation in rocks. *Geophys. Res. Lett.* 6, 1–4.

Winkler, K.W., and Plona, T.J. (1982). Technique for measuring ultrasonic velocity and attenuation spectra in rocks under pressure. *J. Geophys. Res. Solid Earth* 87, 10776–10780.

Winkler, K., Nur, A., and Gladwin, M. (1979). Friction and seismic attenuation in rocks. *Nature* 277, 528–531.